Supplementary information for

Oxide-ion Conductivity Optimization in $BiVO_4$ Scheelite by Acceptor Doping Strategy

Xiaoyan Yang[1,*], *Xiaoling Zeng*[1], *Xing Ming*[2], *Li Yang*[1], *Alberto J. Fernández-Carrión*[1,*], *Sihao Deng*[3], *Lunhua He*[3,4,5], *Xiaojun Kuang*[1,6]

[1]*MOE Key Laboratory of New Processing Technology for Nonferrous Metal and Materials, Guangxi Key Laboratory of Optical and Electronic Materials and Devices, College of Materials Science and Engineering, Guilin University of Technology, Guilin 541004, P. R. China.*

[2]*College of Science, Guilin University of Technology, Guilin 541004, P. R. China.*

[3] *Spallation Neutron Source Science Center, Dongguan 523803, P. R. China*

[4] *Beijing National Laboratory for Condensed Matter Physics, Institute of Physics, Chinese Academy of Sciences, Beijing 100190, P. R. China*

[5.] *Songshan Lake Materials Laboratory, Dongguan 523808, P. R. China*

[6] *College of Chemistry and Bioengineering, Guilin University of Technology, Guilin 541004, P. R. China.*

* E-mail: yangxy@glut.edu.cn, alberto@glut.edu.cn

Supplementary Figures and Tables

Supplementary Table 1. Interatomic potential parameters. The maximum short-range potential cutoff is 12.0 Å.

Buckingham potential					
Interaction	*A* (eV)	*ρ* (Å)	*C* (eV Å^6)	*Y* (e)	*K* (eV Å^{-2})
Mg^{2+} – O^{2-} [1]	2457.2	0.261	0	0.42	349.95
Ca^{2+} – O^{2-} [2]	1228.9	0.3372	0	1.26	34.0
Ba^{2+} – O^{2-} [3]	2096.8	0.3384	8	1.848	29.1
Sr^{2+} – O^{2-} [4]	1400	0.35	0	1.33	21.53
Cd^{2+} – O^{2-} [5]	868.3	0.35	0	/	/
Pb^{2+} – O^{2-} [6]	8086.8	0.2649	3.5636	-0.09	21006.5
Pb^{2+} – Pb^{2+} [6]	18912.114	0.3138	2.6	/	/
Ti^{4+} – O^{2-} [3]	2088.11	0.2888	0	2.89	253.6
Si^{4+} – O^{2-} [3]	1162.46	0.2708	0	/	/
Ge^{4+} – O^{2-} [5]	1035.5	0.3464	0	4.88	317.2
Bi^{3+} – O^{2-} [4]	49529.35	0.2223	0	-5.51	359.55
Bi^{3+} – Bi^{3+} [4]	85839.392	0.3284	0	/	/
V^{5+} – O^{2-} [4]	668.8700	0.4095	0	/	/
O^{2-} – O^{2-} [4]	20117.481	0.2192	32	-2.04	6.3

Supplementary Table 2. Comparison of the lattice parameters for undoped and Ca^{2+}, Pb^{2+} and Ge^{4+}-doped $BiVO_4$ obtained by DFT calculations and experimental refinement. The experimental data were obtained from XRD refinements, excepting the Ca^{2+} doped sample (NPD data).

Compound	Parameters	Calculated	Experimental	(Cal.-Exp.)
	a (Å)	5.255	5.196	0.059
undoped	*b* (Å)	5.255	5.094	0.162
$BiVO_4$	*c* (Å)	11.587	11.705	-0.118
	V (Å^3)	319.99	309.82	10.17
	a (Å)	5.228	5.131	0.097
Ca^{2+} doped	*b* (Å)	5.178	5.131	0.047
$BiVO_4$	*c* (Å)	11.644	11.711	-0.066
	V (Å^3)	315.20	308.31	6.89
	a (Å)	5.332	5.194	0.137
Pb^{2+} doped	*b* (Å)	5.333	5.102	0.231
$BiVO_4$	*c* (Å)	11.517	11.730	-0.213
	V (Å^3)	327.48	310.84	16.64
	a (Å)	5.251	5.180	0.071
Ge^{4+} doped	*b* (Å)	5.185	5.105	0.079
$BiVO_4$	*c* (Å)	11.656	11.700	-0.044
	V (Å^3)	317.33	309.40	7.93

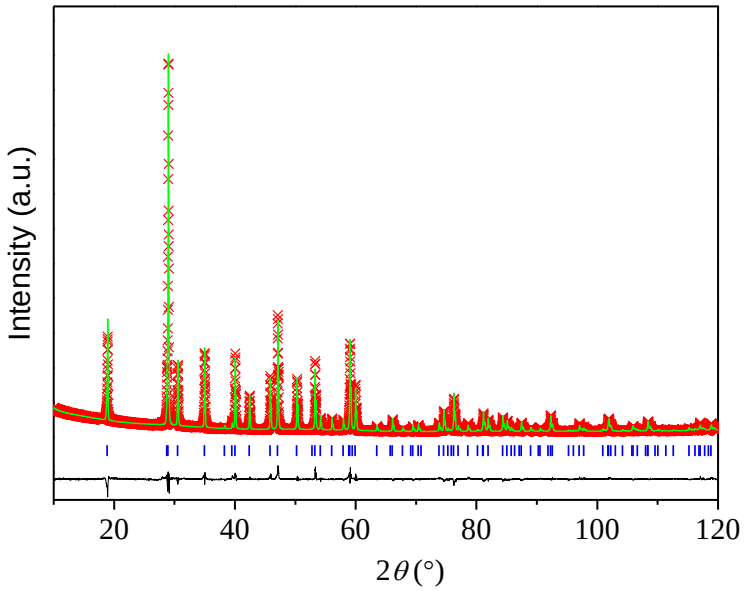

Supplementary Figure 1. Rietveld plots of XRD data of the *t*-$Bi_{0.85}Ca_{0.15}VO_{3.925}$ composition. The reliability factors are R_{wp} ~ 5.80 %, R_p ~ 4.12 % and *GOF* ~ 2.38.

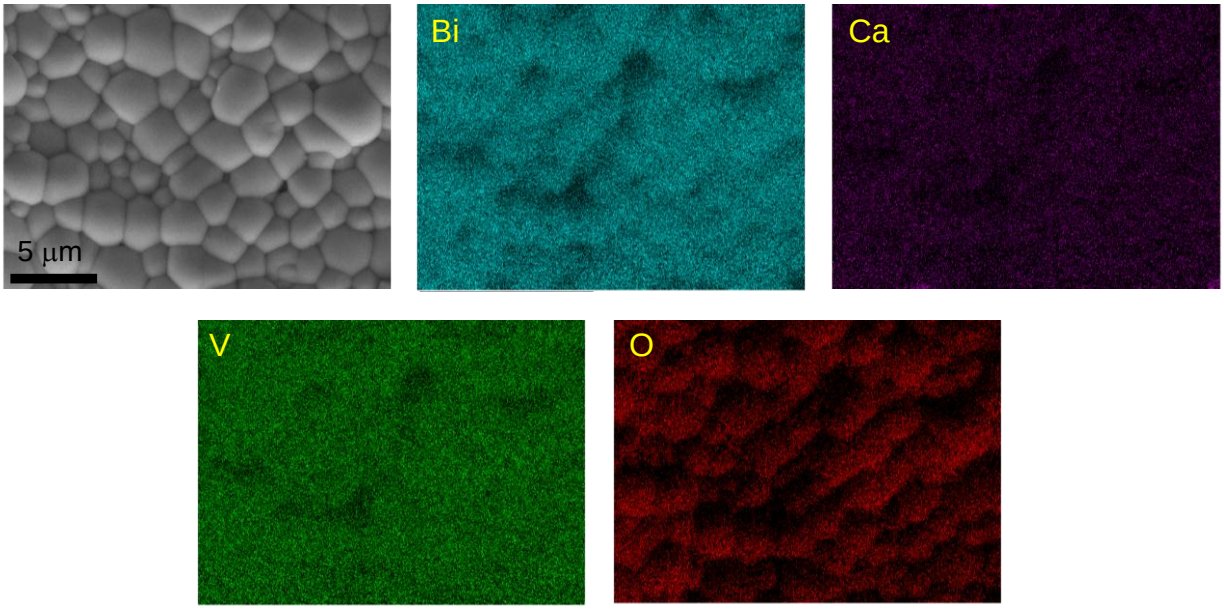

Supplementary Figure 2. The typical SEM-EDS elemental mapping images of $Bi_{0.85}Ca_{0.15}VO_{3.925}$ pellet obtained via heating at 750 ℃ for 10h. The EDS elemental analysis on the grains gave an average cationic composition of $Bi_{0.86(1)}Ca_{0.14(7)}V$, consistent with the theoretical stoichiometric ratio.

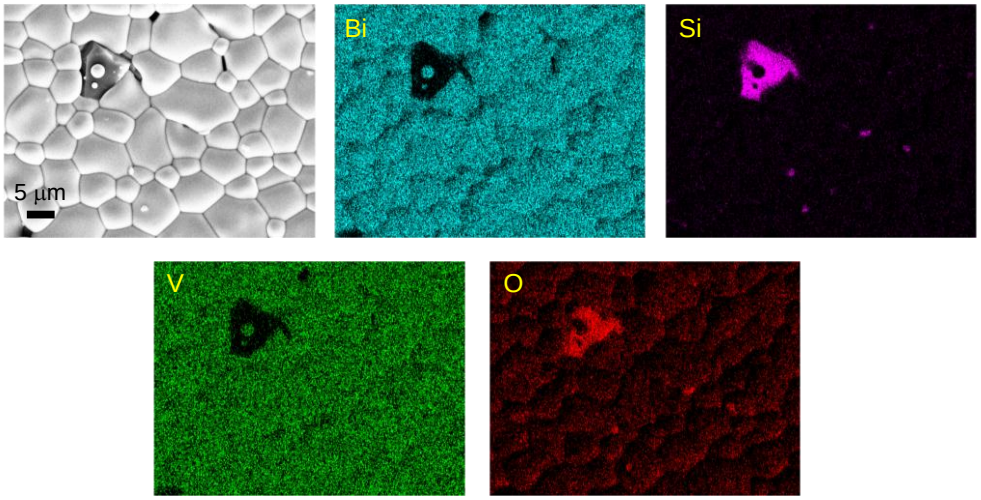

Supplementary Figure 3. SEM-EDS elemental mapping of 1 mol % Si^{4+} replaced V^{5+} in $BiVO_4$.

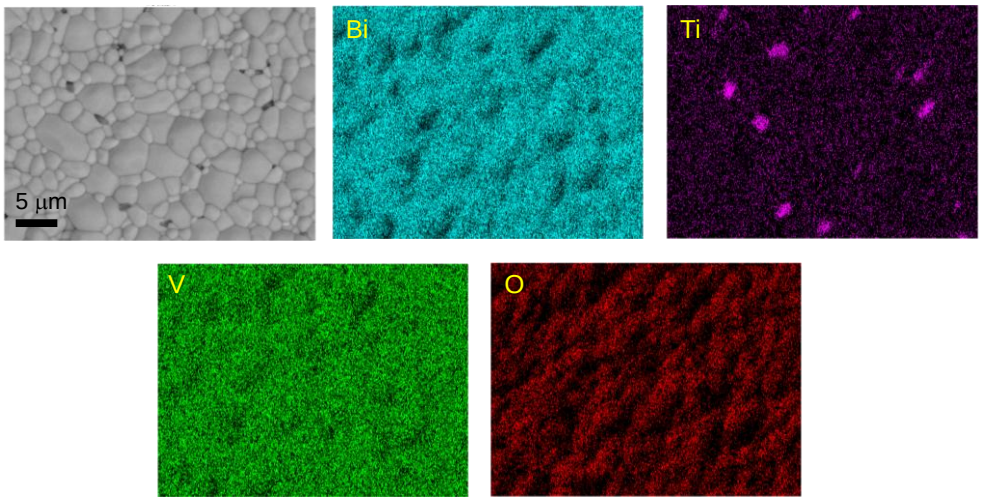

Supplementary Figure 4. SEM-EDS elemental mapping of 1 mol % Ti^{4+} substituted V^{5+} in $BiVO_4$.

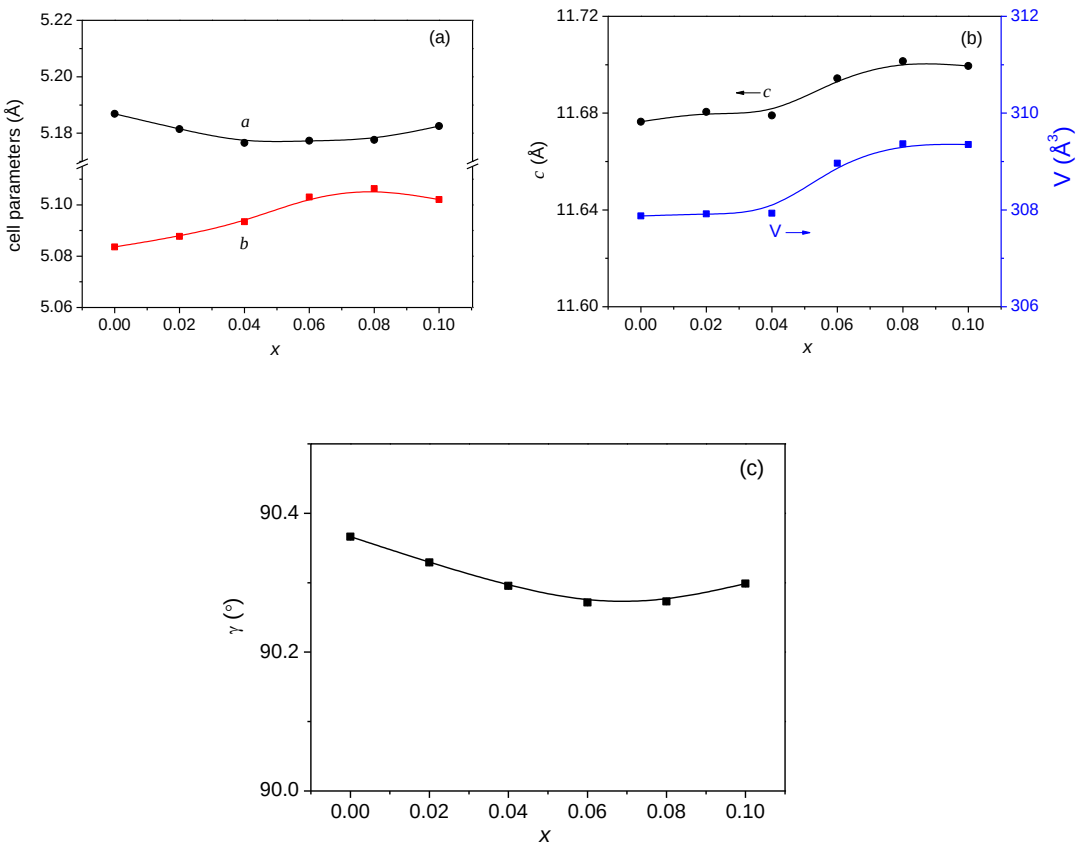

Supplementary Figure 5. The x dependency of the lattice parameters in $BiV_{1-x}Ge_xO_{4-0.5x}$ (x = 0-0.1) samples.

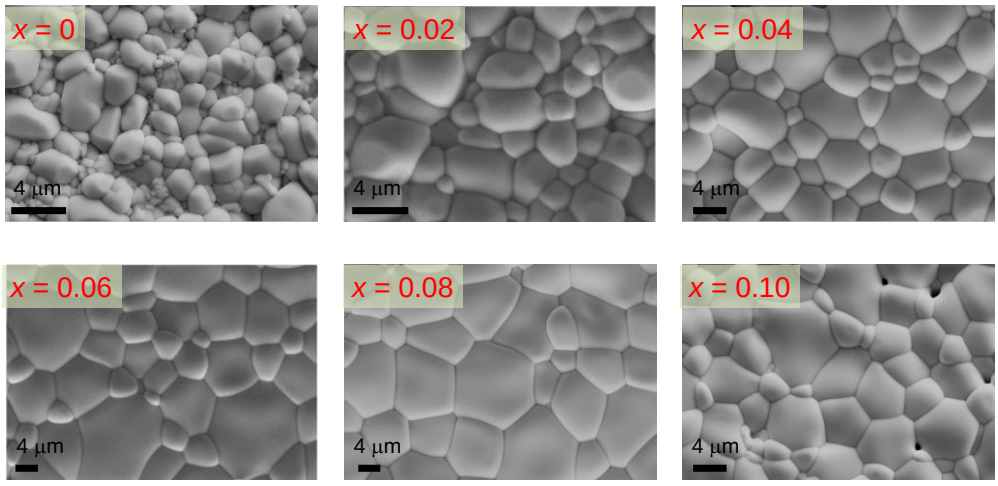

Supplementary Figure 6. The surface morphology of the $Bi_{1-x}Ge_xVO_{4-0.5x}$ (x = 0, 0.02, 0.04, 0.06, 0.08 and 0.1) ceramic pellets.

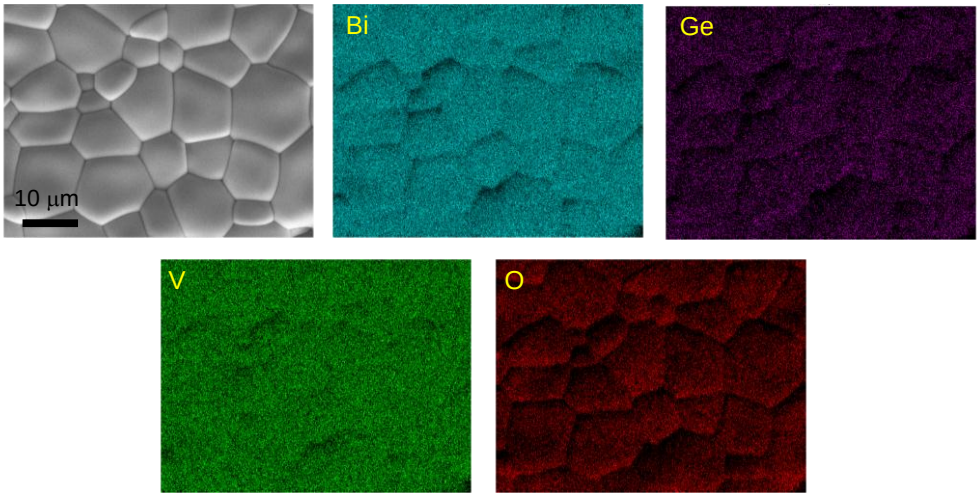

Supplementary Figure 7. SEM-EDS elemental mapping of $BiV_{0.92}Ge_{0.08}O_{3.96}$ ceramic pellet.

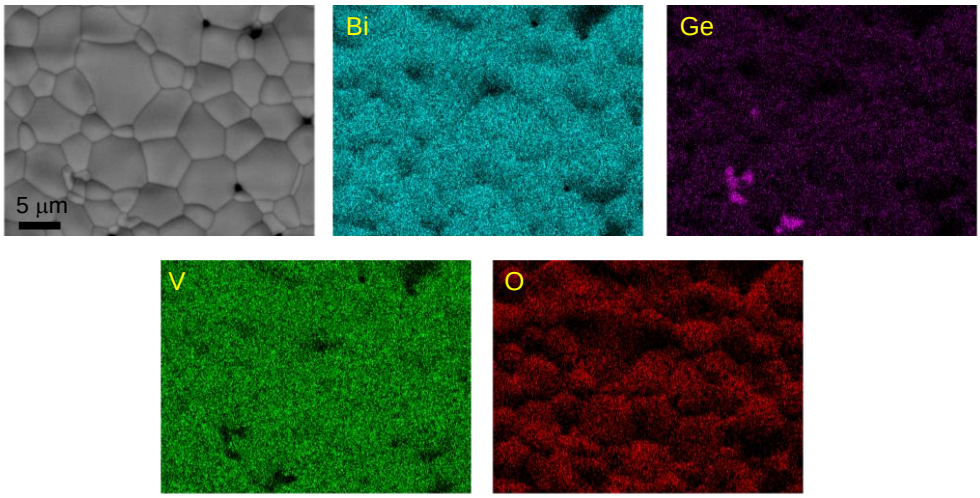

Supplementary Figure 8. SEM-EDS elemental mapping of $BiV_{0.9}Ge_{0.1}O_{3.95}$ ceramic pellet.

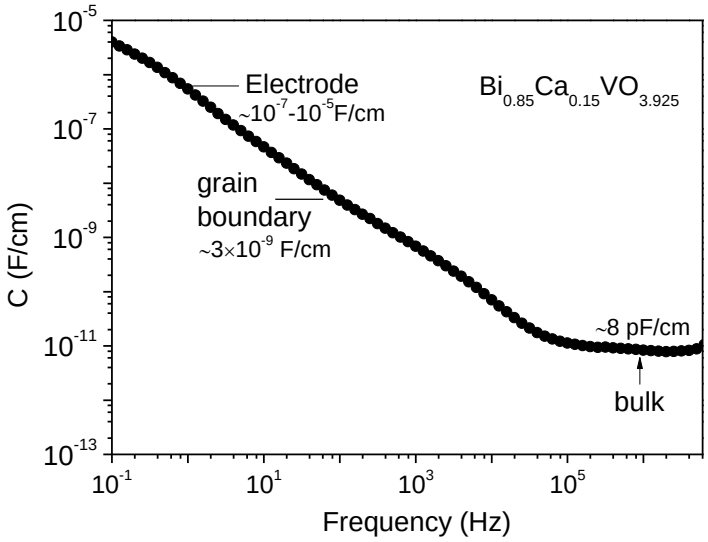

Supplementary Figure 9. The frequency dependency of capacitance for $Bi_{0.85}Ca_{0.15}VO_{3.925}$ ceramic at 300 °C.

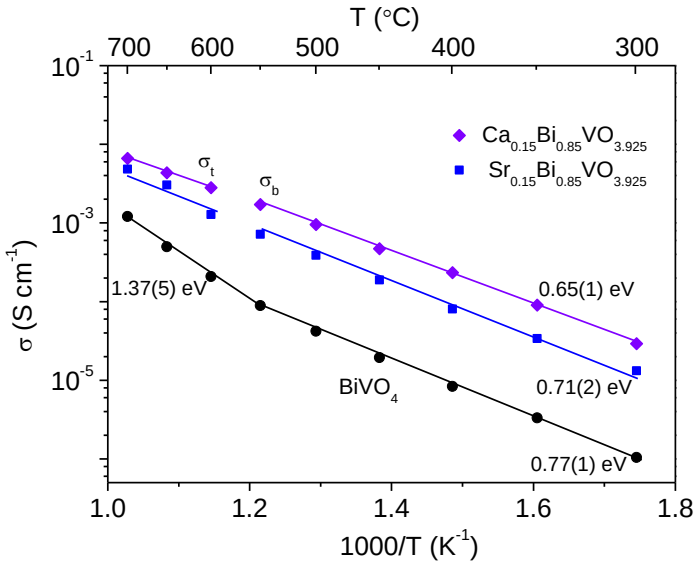

Supplementary Figure 10. Arrhenius plot of the conductivities for tetragonal scheelite $Bi_{0.85}Ca_{0.15}VO_{3.925}$ prepared by solid state method and $Bi_{0.85}Sr_{0.15}VO_{3.925}$ prepared by aerodynamic-levitation method.

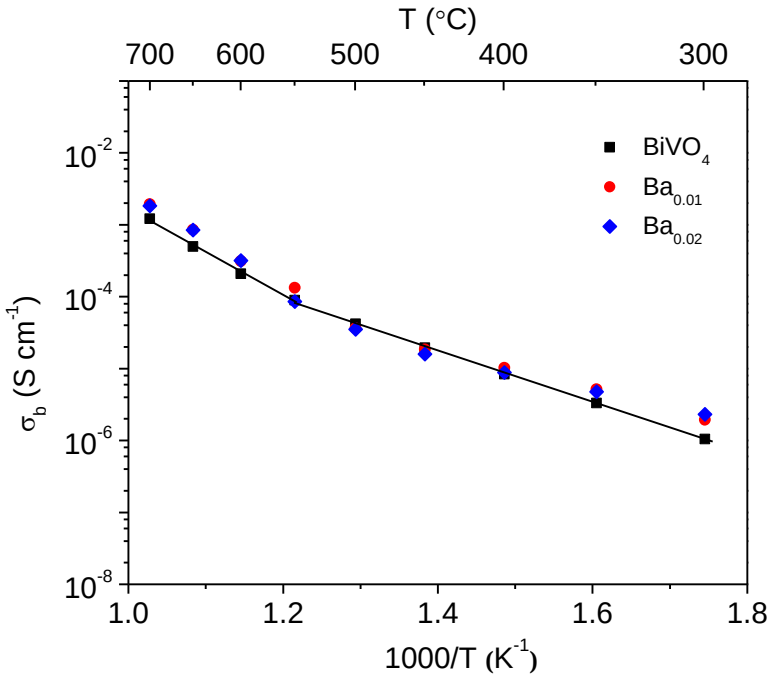

Supplementary Figure 11. Arrhenius plot of the bulk conductivities for $Bi_{1-x}Ba_xVO_{4-0.5x}$ (x = 0, 0.01, 0.02) in air at 300−700 ℃.

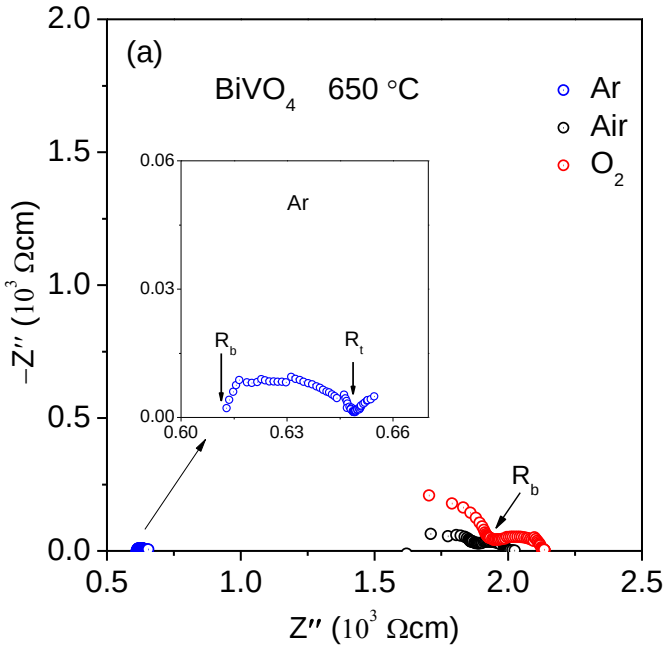

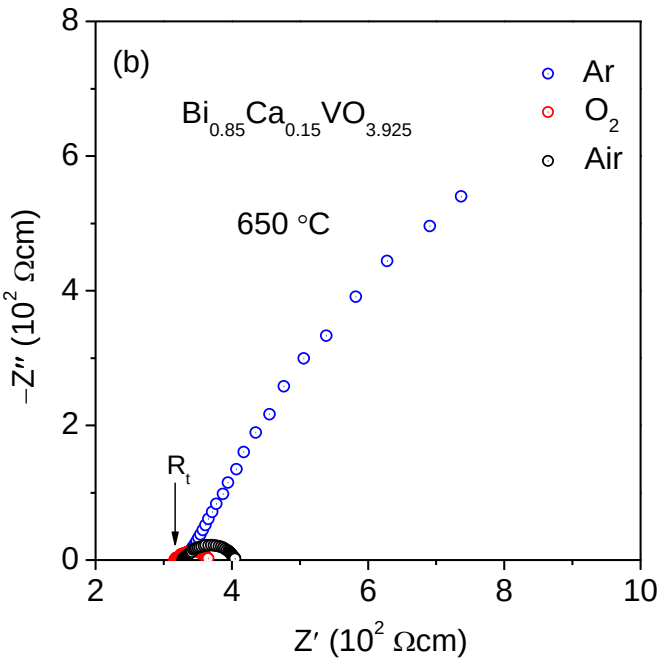

Supplementary Figure 12. Complex impedance plots of (a) $BiVO_4$ and (b) $Bi_{0.85}Ca_{0.15}VO_{3.925}$ pellet recorded at 650 ℃ under air, O_2 and Ar atmosphere. The inset in (a) enlarges the plot under Ar flow. R_b and R_t donate bulk and total resistivities, respectively.

Supplementary Table 3. Oxygen transport number t_{O2-} values of $Bi_{1-x}A_xVO_{4-0.5x}$ (A = Ca-Ba, Pb, Cd) and $BiV_{0.92}Ge_{0.08}O_{3.96}$ at 500 ℃ and 700 ℃, respectively.

Material	T(℃)	EMF (O_2 ‖ air) (mV)		t(O_2 ‖ air)	EMF (Ar ‖ air) (mV)		t(Ar ‖ air)
		Measured	Calculated		Measured	Calculated	
$BiVO_4$	500	-7.2	-26.0	0.28	7.8	127.4	0.06
	700	-4.0	-32.7	0.12	16.2	160.3	0.10
$Bi_{0.85}Ca_{0.15}VO_{3.925}$	500	-24	-26.0	0.92	34	127.4	0.26
	700	-30.5	-32.7	0.93	40.5	160.3	0.25
$Bi_{0.98}Ba_{0.02}VO_{3.99}$	500	-11	-26.0	0.42	17	127.4	0.13
	700	-12	-32.7	0.37	16.5	160.3	0.10
$Bi_{0.94}Pb_{0.06}VO_{3.97}$	500	-20.2	-26.0	0.78	30.5	127.4	0.24
	700	-26.5	-32.7	0.81	32	160.3	0.20
$Bi_{0.94}Cd_{0.06}VO_{3.97}$	500	-22.2	-26.0	0.85	26.5	127.4	0.21
	700	-28	-32.7	0.86	31.7	160.3	0.20
$BiV_{0.92}Ge_{0.08}O_{3.96}$	500	-17.7	-26.0	0.68	31.0	127.4	0.24
	700	-24.1	-32.7	0.74	36.0	160.3	0.22
$Bi_{0.9}Sr_{0.1}VO_{3.95}$ [4]	500	-23.2	-26.0	0.87	62.6	127.4	0.49
	700	-29.2	-32.7	0.86	53.4	160.3	0.33

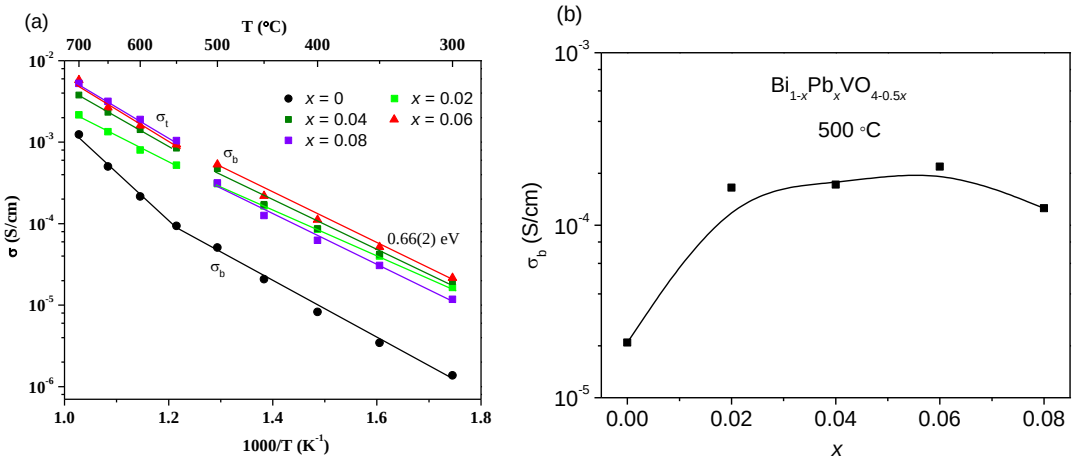

Supplementary Figure 13. (a) Arrhenius plot of the conductivities for $Bi_{1-x}Pb_xVO_{4-0.5x}$ (x = 0-0.08) in air at 300-700 ℃, (b) The x dependency of the bulk conductivities for $Bi_{1-x}Pb_xVO_{4-0.5x}$ (x = 0-0.08) in air at 500 ℃.

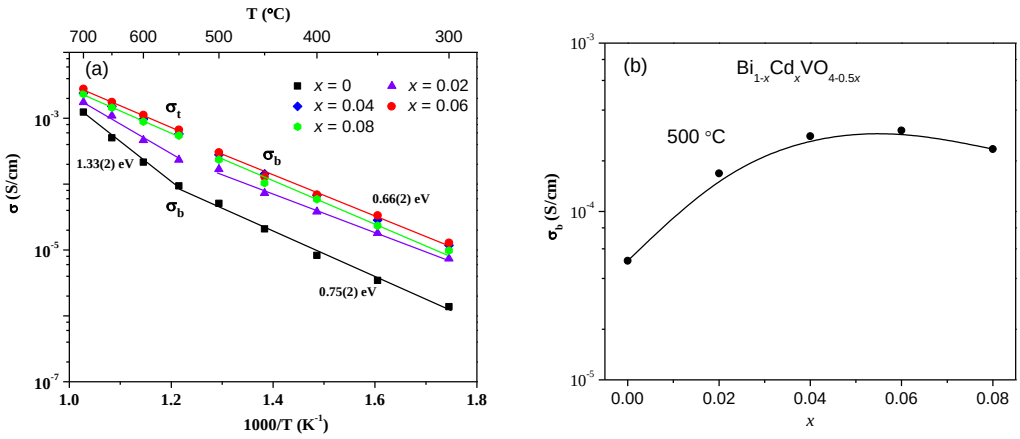

Supplementary Figure 14. (a) Arrhenius plot of the conductivities for $Bi_{1-x}Cd_xVO_{4-0.5x}$ (x = 0-0.08) in air at 300-700 ℃, (b) The x dependency of the bulk conductivities for $Bi_{1-x}Cd_xVO_{4-0.5x}$ (x = 0-0.08) in air at 500 ℃.

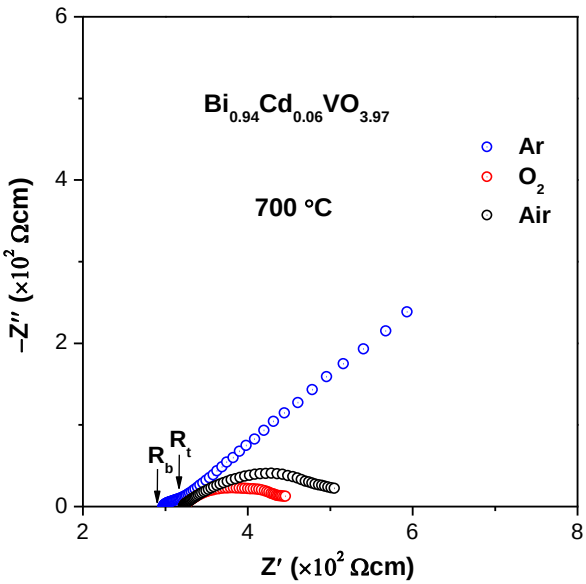

Supplementary Figure 15. Complex impedance plots of $Bi_{0.94}Cd_{0.06}VO_{3.97}$ pellet recorded at 700 ℃ under air, O_2 and Ar atmosphere. R_b and R_t donate bulk and total resistivities, respectively.

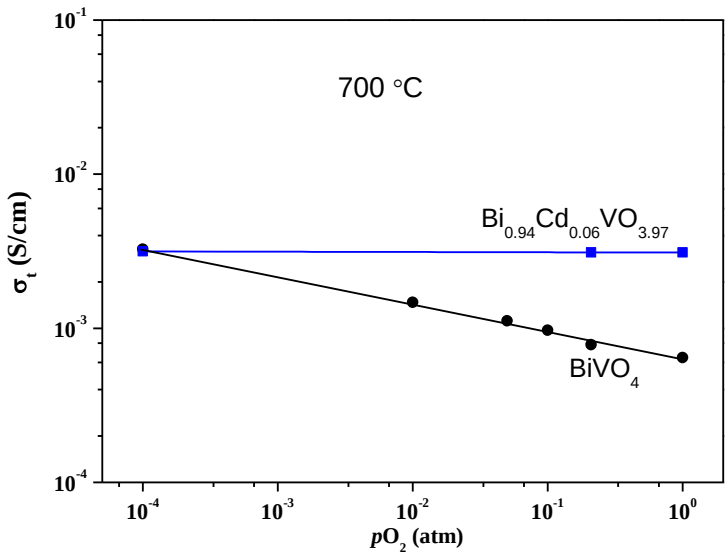

Supplementary Figure 16. The pO_2 dependency of the conductivity of $BiVO_4$ and $Bi_{0.94}Cd_{0.06}VO_{3.97}$ at 700 ℃.

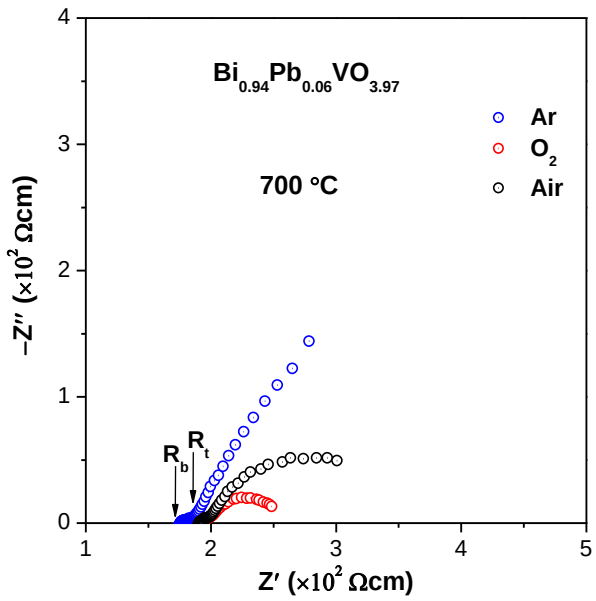

Supplementary Figure 17. Complex impedance plots of $Bi_{0.94}Pb_{0.06}VO_{3.97}$ ceramics at 700 ℃ under air, O_2 and Ar atmosphere. R_t and R_t donate bulk and total resistivity, respectively.

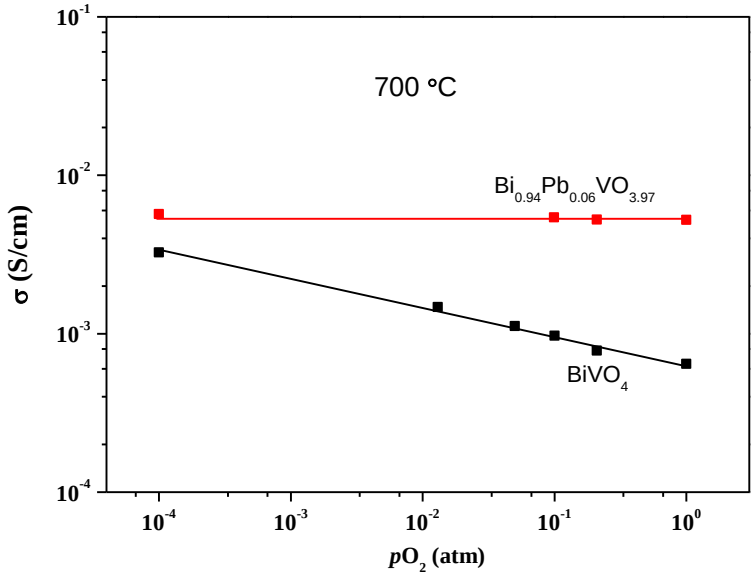

Supplementary Figure 18. The pO_2 dependency of the conductivity of $BiVO_4$ and $Bi_{0.94}Pb_{0.06}VO_{3.97}$ at 700 ℃.

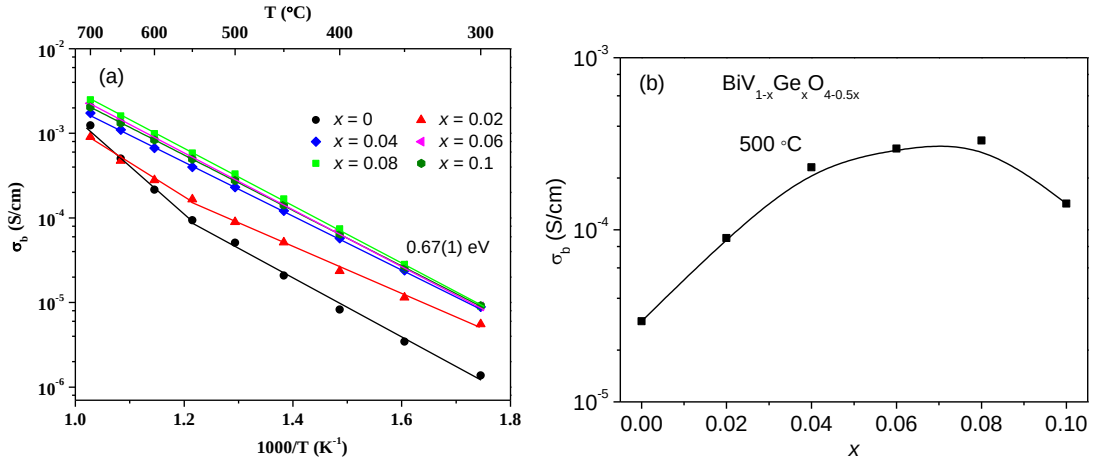

Supplementary Figure 19. (a) Arrhenius plot of the conductivities for $BiV_{1-x}Ge_xO_{4-0.5x}$ (x = 0-0.1) in air at 300-700 ℃, (b) The x dependency of the bulk conductivities for $BiV_{1-x}Ge_xO_{4-0.5x}$ (x = 0-0.1) in air at 500 ℃.

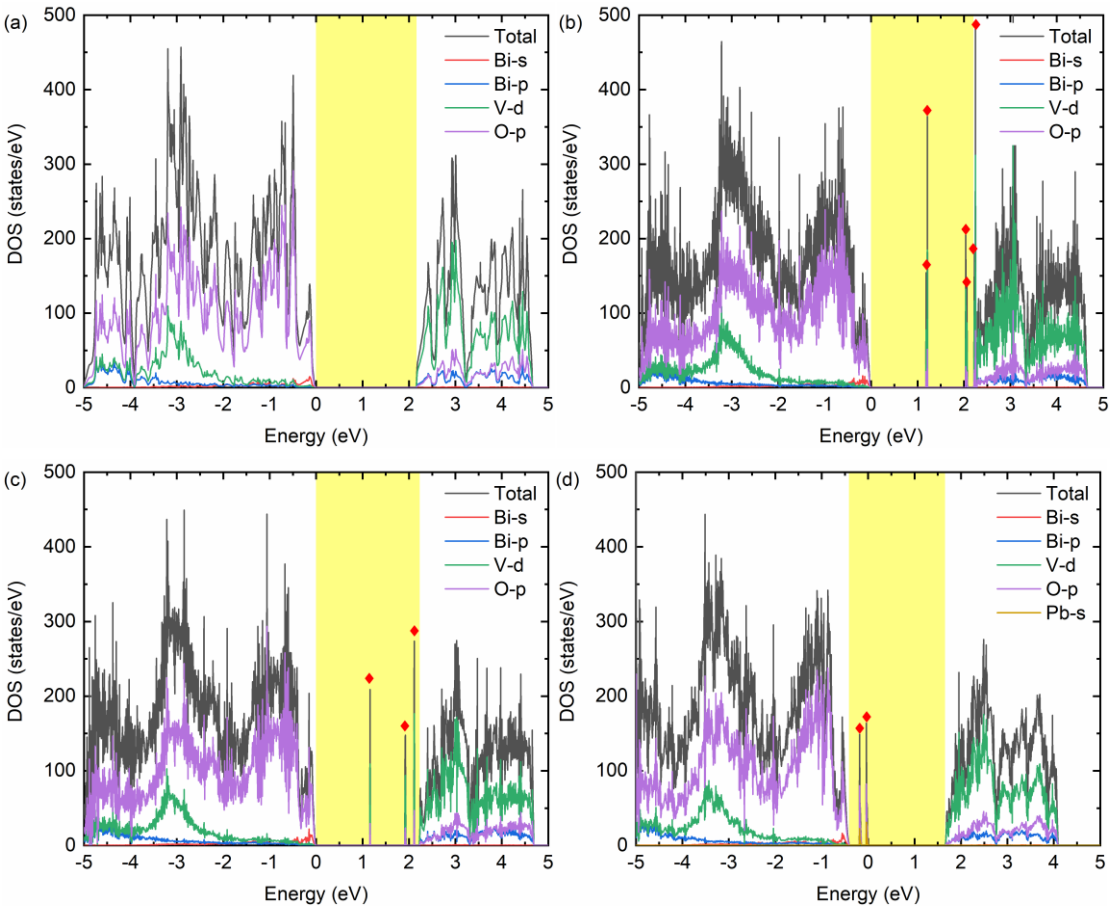

Supplementary Figure 20. Total and partial density of states (DOS) of the (a) intrinsic $BiVO_4$ system and with dopants of (b) Ca^{2+}, (c) Ge^{4+}, and (d) Pb^{2+}. The defect levels are marked with the red diamonds. The yellow shaded regions denote the intrinsic band gaps in each case.

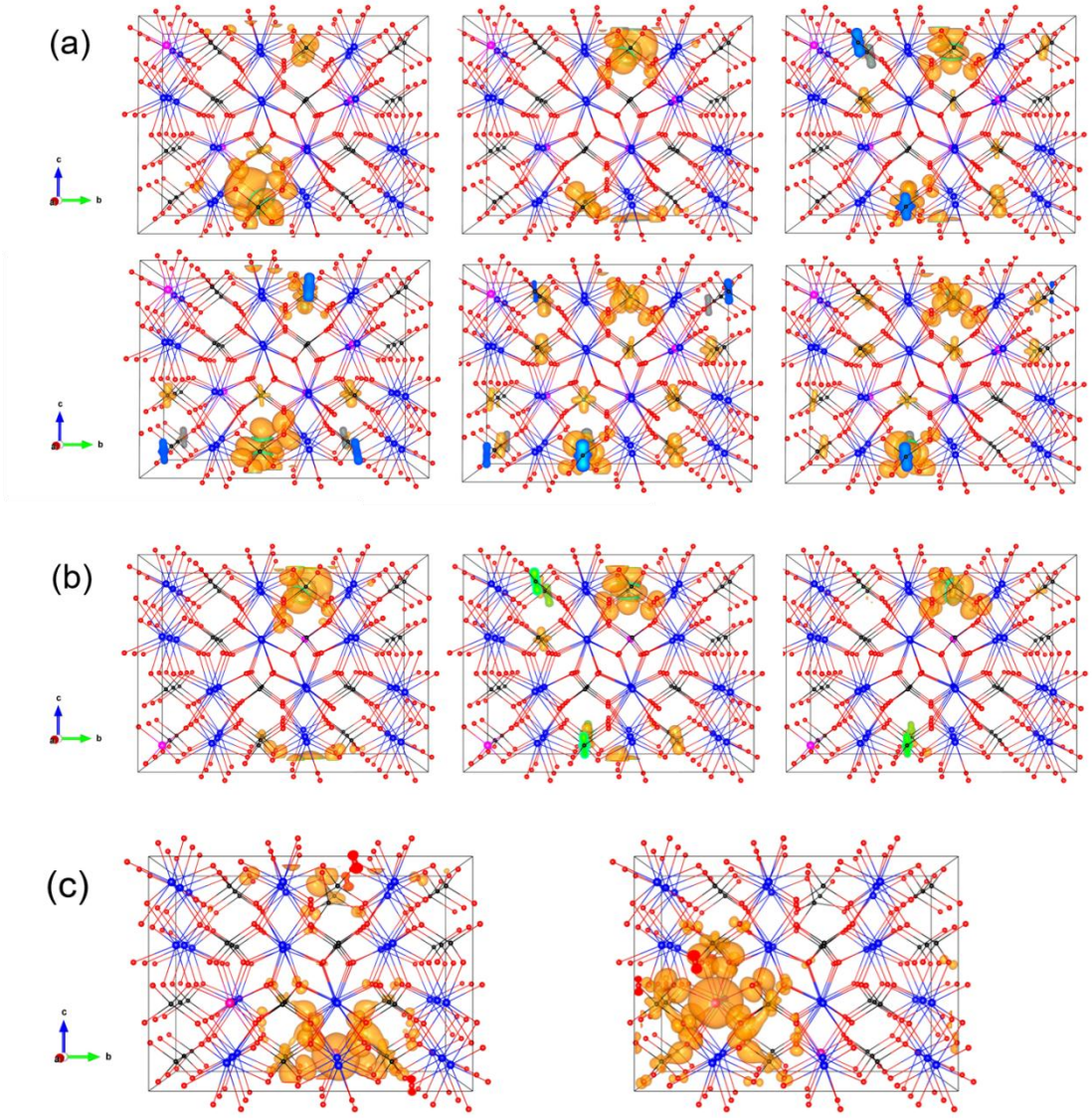

Supplementary Figure 21. The partial charge densities of the defect levels for (a) Ca^{2+}, (b) Ge^{4+}, and (c) Pb^{2+} acceptors doped $BiVO_4$, which corresponds to the defect levels marked by the red diamonds in **Supplementary Figure 20**.

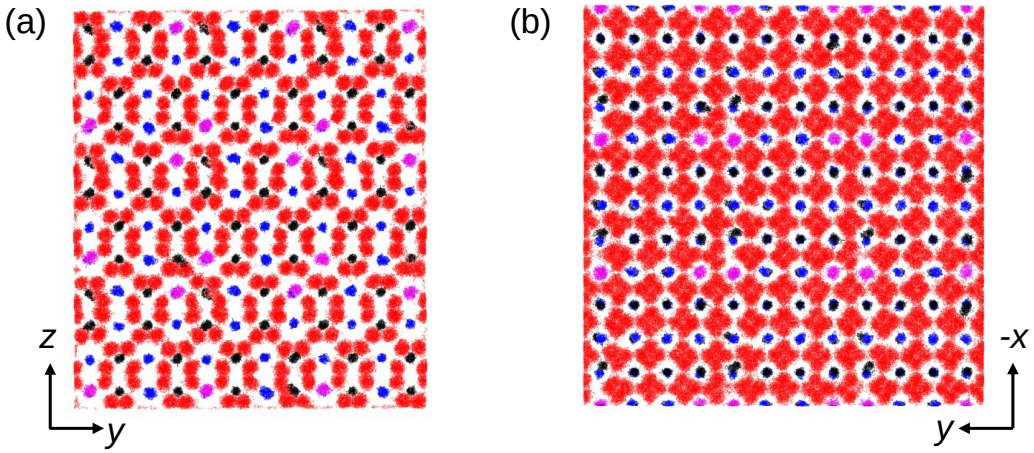

Supplementary Figure 22. Trajectory scatter plots along (a) (100) and (b) (001) planes of $Bi_{0.875}Ca_{0.125}VO_{3.9375}$ at 1700 ℃ from the MD simulations. The blue, magenta, black and red dots represent Bi, Ca, V and O atoms respectively.

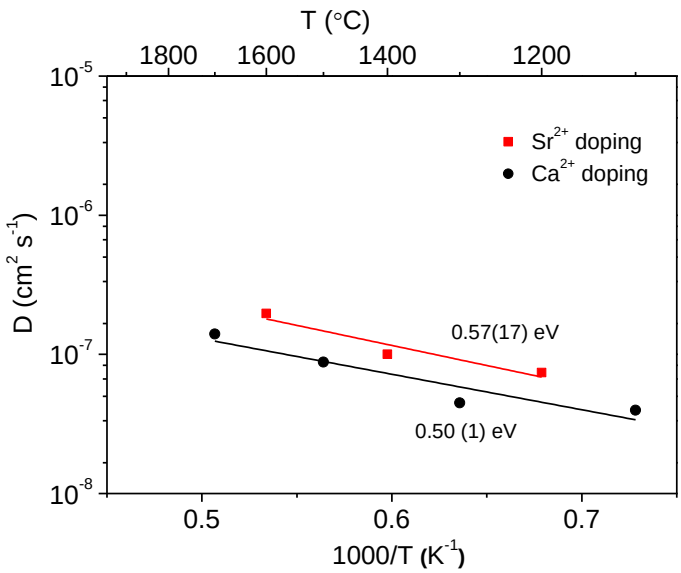

Supplementary Figure 23. Arrhenius plot of the oxygen diffusion coefficient for $Bi_{0.875}Ca_{0.125}VO_{3.9375}$ composition calculated using the MSD values of oxygen atoms within 1100-1700 °C temperature range. The value of Sr-doped sample we reported is shown for comparison.[4] The activation energy of MSD is labeled.

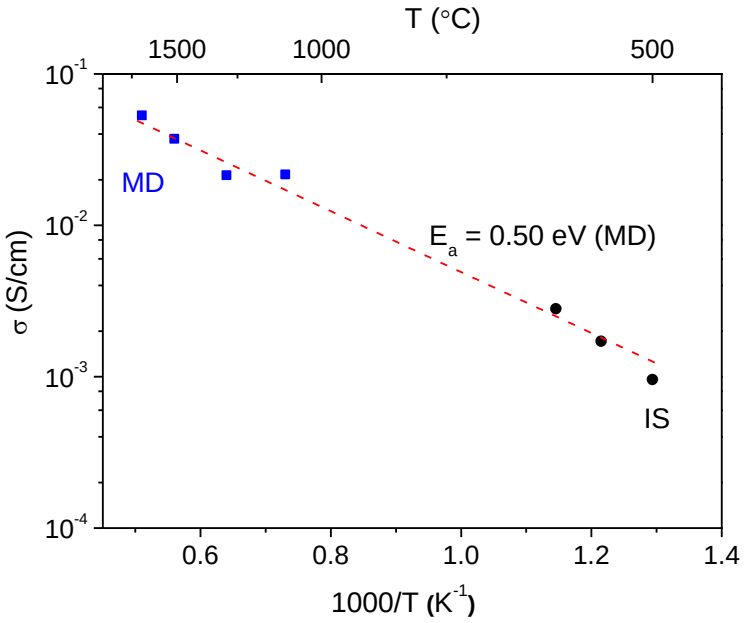

Supplementary Figure 24. Comparison of the oxide ion conductivities for $Bi_{0.875}Ca_{0.125}VO_{3.9375}$ obtained by impedance spectroscopy (black solid circle) and MD simulations (blue solid square).

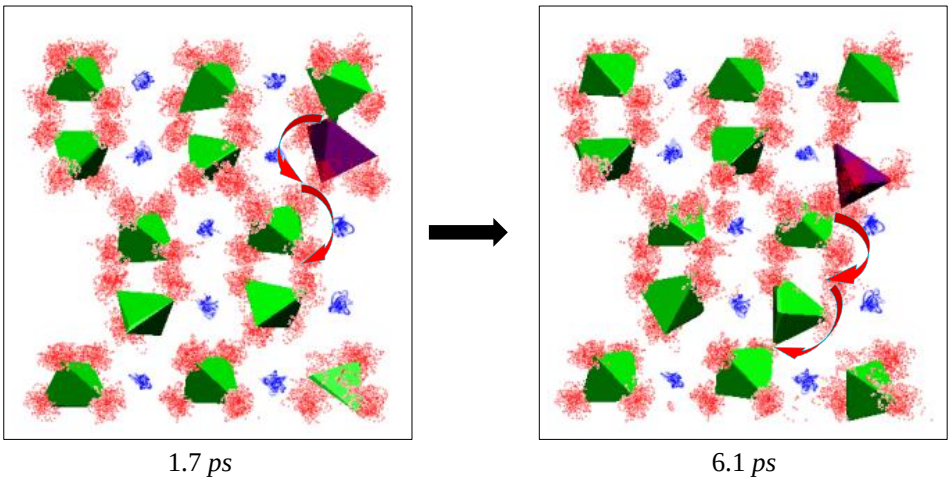

Supplementary Figure 25. Trajectory scatter plots of Bi and O atoms showing the oxygen vacancy migration path involving the $(V/Ge)_2O_7$ dimer breaking and reforming for $BiV_{0.94}Ge_{0.06}O_{3.97}$ at 2300 ℃. The blue and red dots represent Bi and O atoms, the purple and green tetrahedron denotes GeO_4 and VO_4 unit, respectively. The red arrows show the direction for the oxygen vacancy migration path.

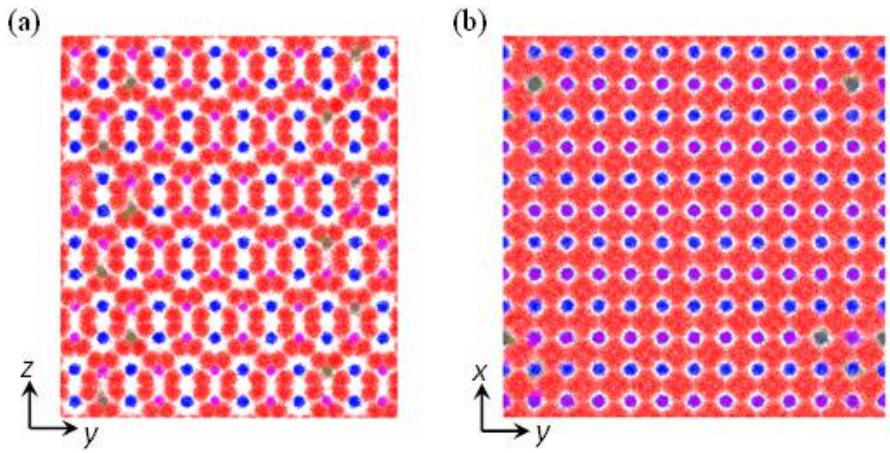

Supplementary Figure 26. Trajectory scatter plots along (a) (100) and (b) (001) planes of $BiV_{0.94}Ge_{0.06}O_{3.97}$ at 2300 ℃ from the MD simulations. The blue, magenta, olive and red dots represent Bi, V, Ge and O atoms respectively.

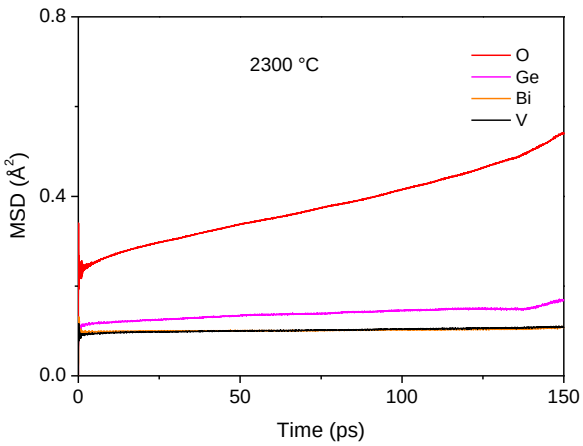

Supplementary Figure 27. MSD values of Bi, V, Ge and O atoms as a function of time from the MD simulation at 2300 °C for $BiV_{0.94}Ge_{0.06}O_{3.97}$.

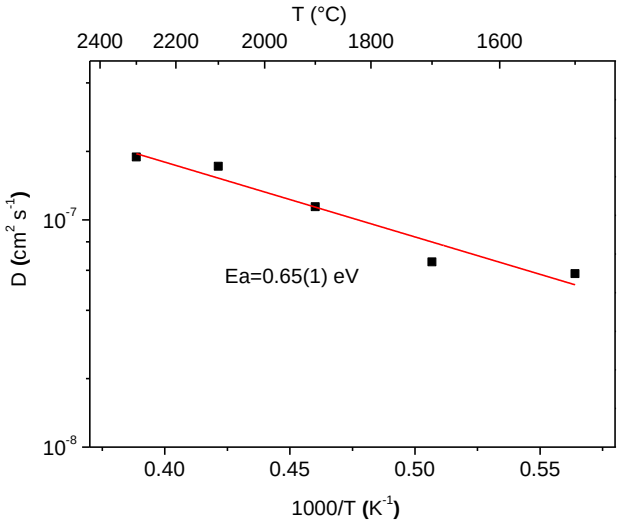

Supplementary Figure 28. Arrhenius plot of the oxygen diffusion coefficient for $BiV_{0.94}Ge_{0.06}O_{3.97}$ composition calculated using the MSD values of oxygen atoms within 1500-2300 °C temperature range. The activation energy of Mean square displacement values is labeled.

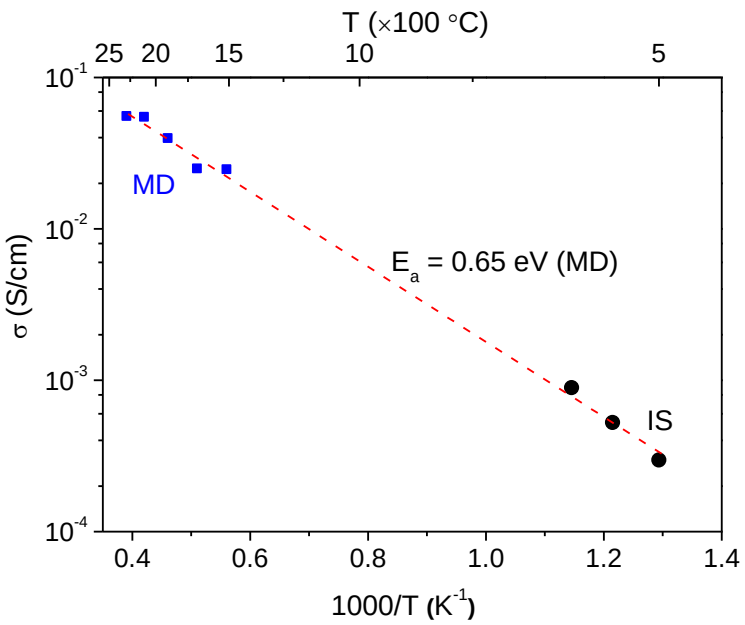

Supplementary Figure 29. Comparison of the oxide ion conductivities for $BiV_{0.94}Ge_{0.06}O_{3.97}$ obtained by impedance spectroscopy (black solid circle) and MD simulations (blue solid square).

Supplementary Notes

Supplementary Note 1. *A* solubility and phase formation in $Bi_{1-x}A_xVO_{4-0.5x}$

Supplementary Figure 30 shows the XRD patterns of $Bi_{1-x}Mg_xVO_{4-0.5x}$ compositions. Secondary phases were not detected within the $0 \leq x \leq 0.15$ compositional range, while $Mg_2V_2O_7$ impurity was observed in $x \geq 0.15$ compositions. However, no reflection position shift was detected upon increasing the doping level, as confirmed by the refined cell parameters evolution (**Supplementary Table 4**). The samples were then analyzed by SEM-EDS (**Supplementary Figure 31**). The data clearly shown a micrometric phase segregation even for the compositions with low doping contents (x = 0.02) where magnesium is intensively segregated in the grains with strip-like shape, being its presence rather limited in the rest of the grains (less than 1%). The elemental analysis in these elongated grains indicates the formation of $MgVO_{3.5}$ that can be assigned to the presence of $Mg_2V_2O_7$ secondary phase. Thus, the data reveals the difficulty of effective magnesium doping within the Scheelite $BiVO_4$.

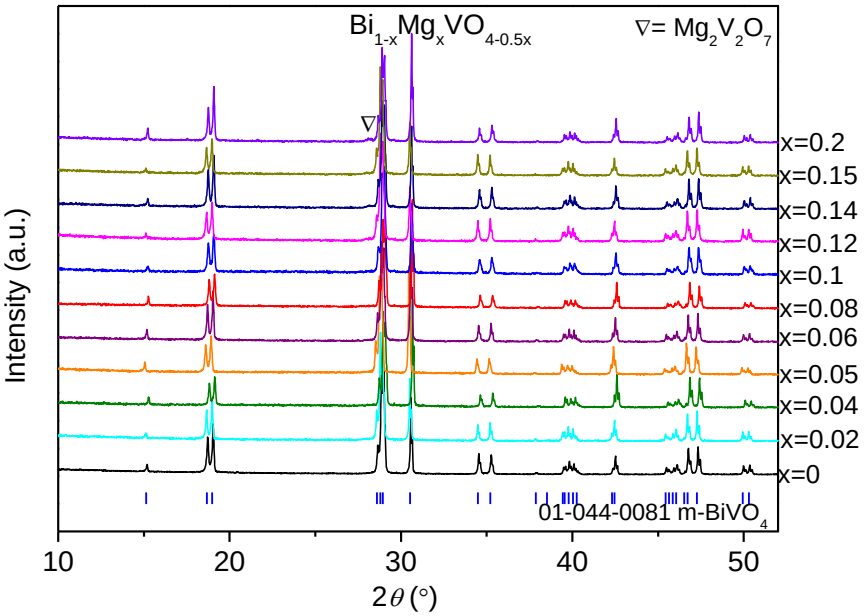

Supplementary Figure 30. XRD patterns of $Bi_{1-x}Mg_xVO_{4-0.5x}$ (x = 0-0.2) samples. The blue vertical ticks denote Bragg reflection positions for the monoclinic $BiVO_4$ (*No.* 01-044-0081) from ICDD database. The ∇ donates the secondary phase $Mg_2V_2O_7$.

Supplementary Table 4. Refined cell parameters of $Bi_{1-x}Mg_xVO_{4-0.5x}$.

Composition	*a* (Å)	*b* (Å)	*c* (Å)	γ (°)	V (Å^3)
$BiVO_4$	5.19654(5)	5.09352(5)	11.7053(1)	90.376(1)	309.82(1)
$Bi_{0.98}Mg_{0.02}VO_{3.99}$	5.19663(6)	5.09281(6)	11.7036(1)	90.376(1)	309.71(1)
$Bi_{0.95}Mg_{0.05}VO_{3.975}$	5.19504(8)	5.09302(8)	11.7036(2)	90.365(1)	309.65(1)
$Bi_{0.9}Mg_{0.1}VO_{3.95}$	5.19579(8)	5.09282(8)	11.7035(2)	90.370(1)	309.68(1)
$Bi_{0.85}Mg_{0.15}VO_{3.92}$	5.19593(8)	5.09301(8)	11.7031(2)	90.373(1)	309.71(1)
$Bi_{0.8}Mg_{0.2}VO_{3.9}$	5.19634(8)	5.09283(8)	11.7031(1)	90.374(1)	309.71(1)

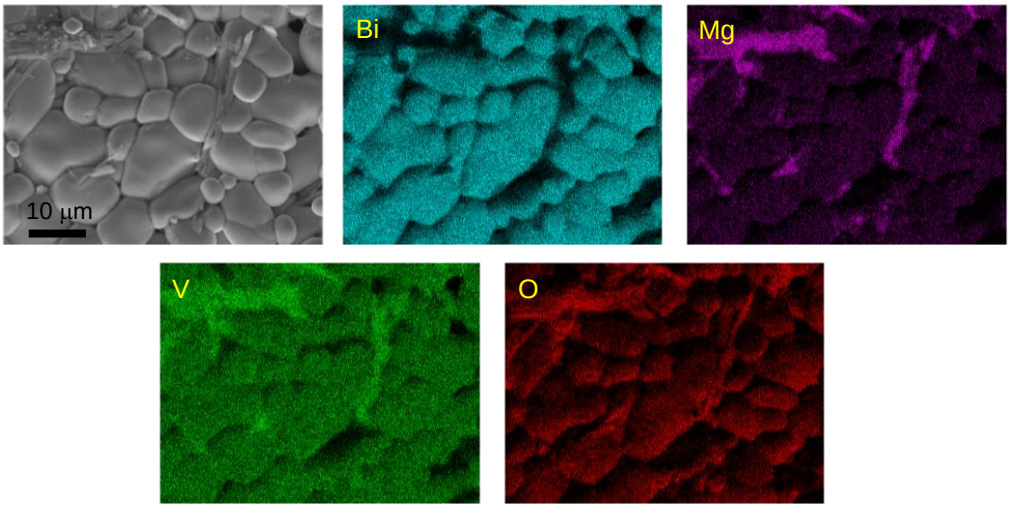

Supplementary Figure 31. Elemental mapping images of Bi, Mg, V and O elements in the 2 mol% Mg^{2+} substituted Bi^{3+} in $BiVO_4$. The grains with strip-like shape arises from the $Mg_2V_2O_7$ secondary phase.

Regarding the Ba^{2+}-doped samples, the single $BiVO_4$ phase was obtained only within x = 0-0.02 compositional range, beyond which the secondary phase $BiBa_2V_3O_{11}$ was observed from the XRD patterns (**Supplementary Figure 32**). The refined cell parameters and SEM-EDS elemental mapping results (**Supplementary Figure 33-35**) clearly indicate that the solid solubility of Ba^{2+} in $BiVO_4$ can be extended only to x = 0.02, *i.e.*, compared with Ca^{2+} and Sr^{2+} doping, the Ba^{2+} substitution for Bi^{3+} in $BiVO_4$ is rather difficult although easier than Mg^{2+} doping.

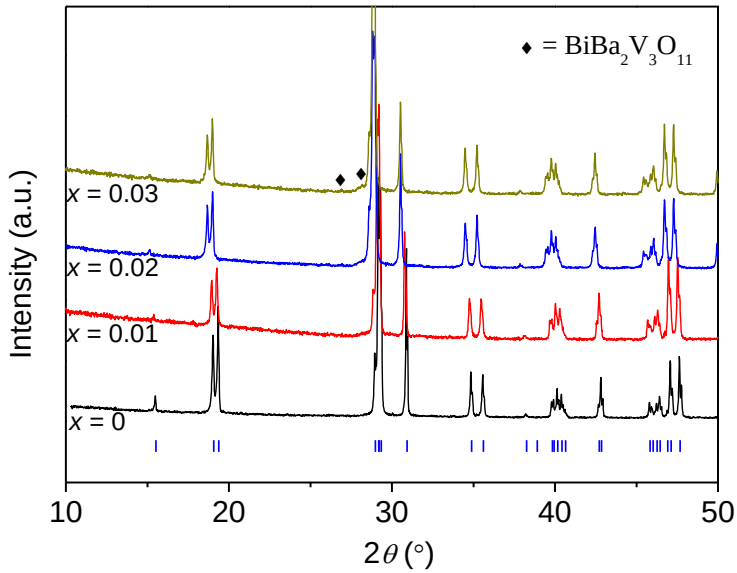

Supplementary Figure 32. XRD patterns of $Bi_{1-x}Ba_xVO_{4-0.5x}$ (x = 0-0.03) samples. The blue vertical ticks denote Bragg reflection positions for the monoclinic $BiVO_4$ (*No.* 01-044-0081) from ICDD database. The ♦ donates the secondary phase $BiBa_2V_3O_{11}$.

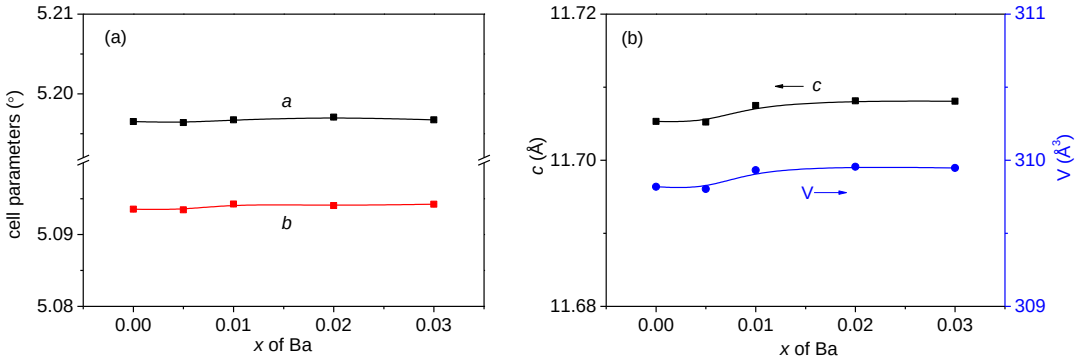

Supplementary Figure 33. The x dependency of the lattice parameters in $Bi_{1-x}Ba_xVO_{4-0.5x}$ (x = 0-0.03) samples.

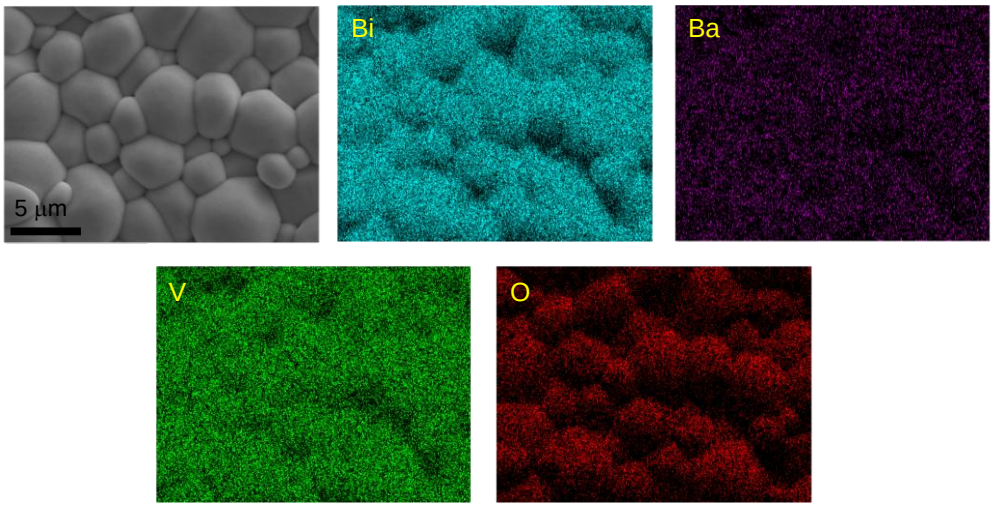

Supplementary Figure 34. Elemental mapping images of Bi, Ba, V and O elements in the $Bi_{0.98}Ba_{0.02}VO_{9.99}$ pellet.

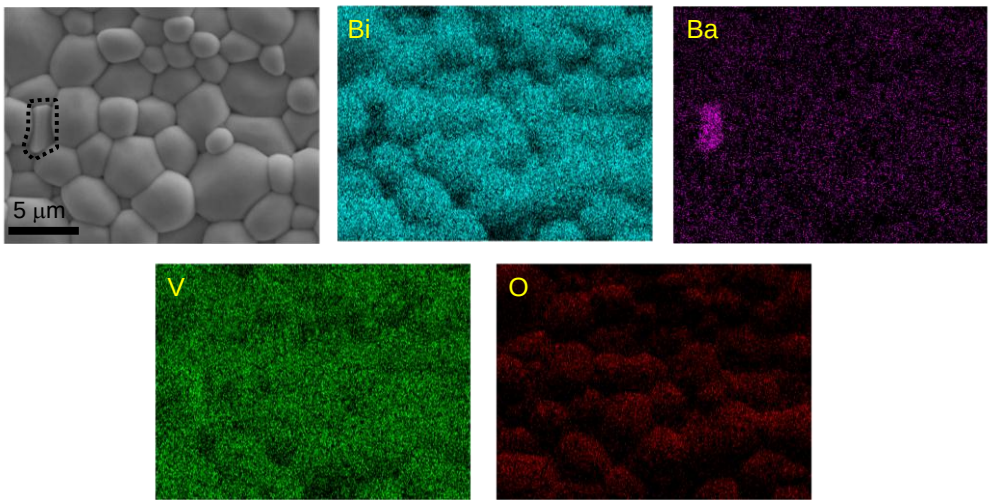

Supplementary Figure 35. Elemental mapping images of Bi, Ba, V and O elements in the $Bi_{0.97}Ba_{0.03}VO_{9.985}$ pellet. The presence of $Ba_2BiV_3O_{11}$ secondary phase has been pointed out by dotted black contour.

Supplementary Figure 36 shows the corresponding XRD patterns recorded for $Bi_{1-x}Cd_xVO_{4-0.5x}$ compounds and indicate the presence of pure monoclinic phase until 8 mole % substitution. Further increase resulted in the formation of $Cd_2V_2O_7$ (PDF 01-078-0951). This result differs to the one reported by Uma et al.[7] who founds a much larger solid solubility range (x = 0.25). The Rietveld analysis of the patterns indicate a progressive decrease of the *a* lattice parameter, while the *b* lattice parameter increases, remaining both parameters constant upon x = 0.08 composition (**Supplementary Figure 37**). The unit cell volume decrease until x = 0.08 due to the smaller ionic size of Cd^{2+}(1.10 Å) compared to Bi^{3+}.The presence of the secondary phase was further confirmed by SEM-EDS (**Supplementary Figure 38-40**) which clearly evidenced the formation of secondary phases for x = 0.1 compound.

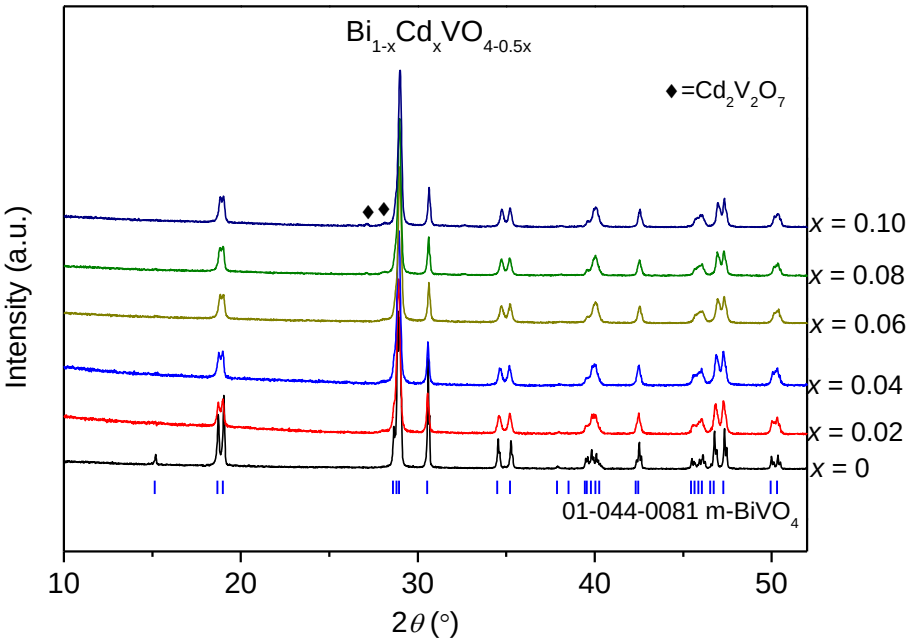

Supplementary Figure 36. XRD patterns of $Bi_{1-x}Cd_xVO_{4-0.5x}$ (x = 0-0.1) samples. The blue vertical ticks denote Bragg reflection positions for the monoclinic $BiVO_4$ (*No.* 01-044-0081) from ICDD database. The ♦ donates the secondary phase $Cd_2V_2O_7$.

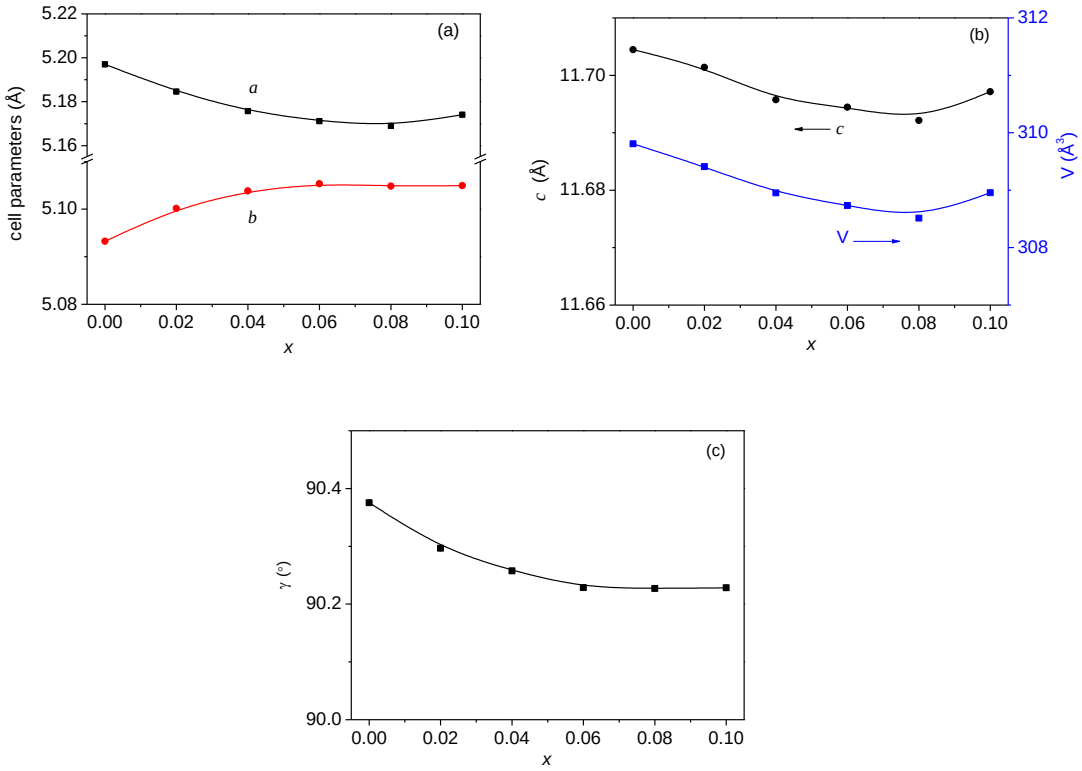

Supplementary Figure 37. The x dependency of the lattice parameters in $Bi_{1-x}Cd_xVO_{4-0.5x}$ (x = 0-0.1).

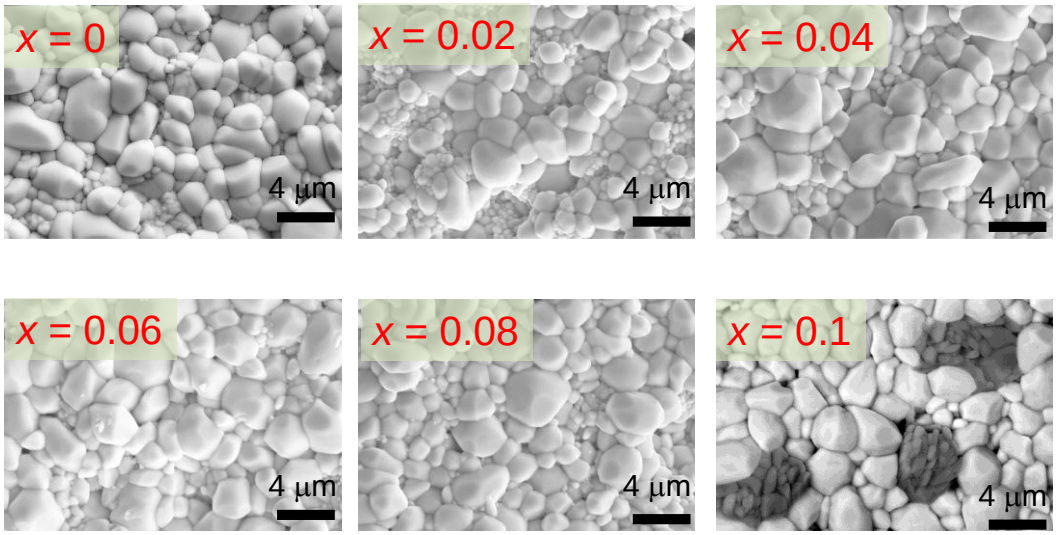

Supplementary Figure 38. The surface morphology of the $Bi_{1-x}Cd_xVO_{4-0.5x}$ (x = 0, 0.02, 0.04, 0.06, 0.08 and 0.1) ceramic pellets.

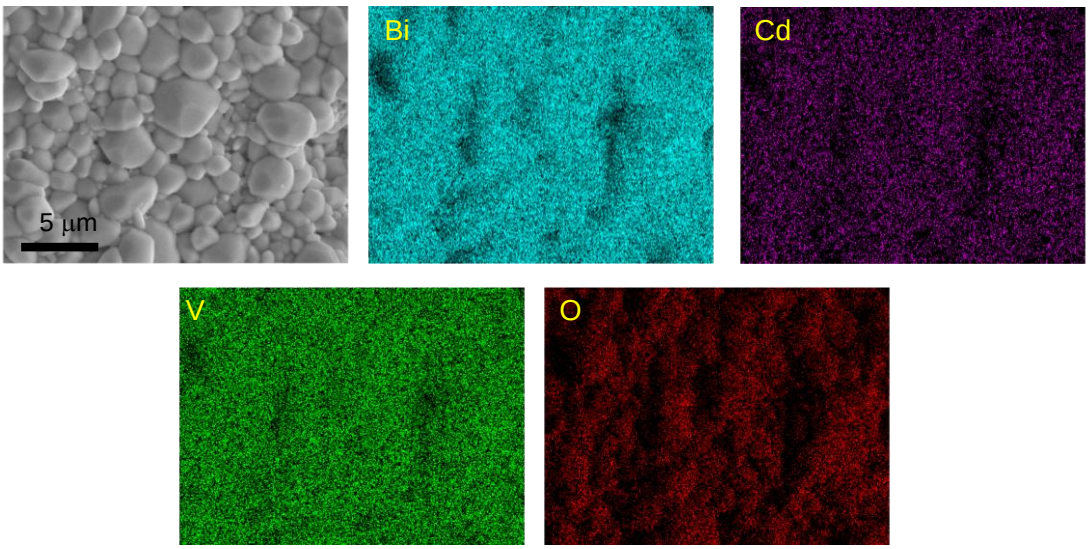

Supplementary Figure 39. SEM-EDS elemental mapping of $Bi_{0.92}Cd_{0.08}VO_{3.96}$ ceramic pellet.

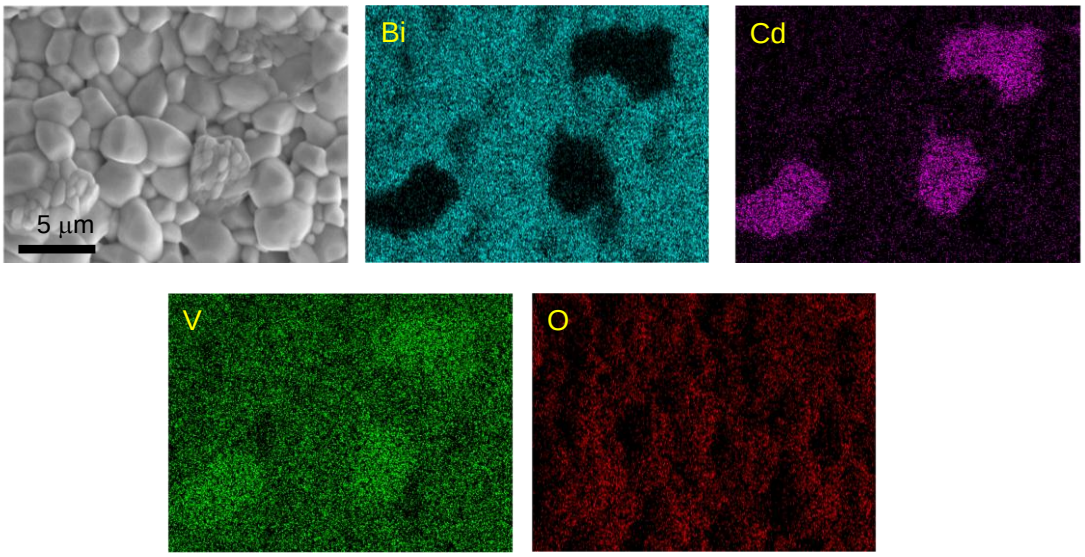

Supplementary Figure 40. SEM-EDS elemental mapping of $Bi_{0.9}Cd_{0.1}VO_{3.95}$ ceramic pellet.

Supplementary Figure 41 shows the corresponding XRD patterns recorded for $Bi_{1-x}Pb_xVO_{4-0.5x}$ compounds and indicate the presence of pure monoclinic phase until 6 mole % substitution. Further increase leads to the formation of $BiPb_2V_3O_{11}$ and thereby the tetragonal Scheelite phase could not be isolated in this system. The Rietveld analysis of the patterns indicate a progressive decrease of the *a* lattice parameter, while the *b* lattice parameter increases. Overall, the unit cell volume increases until x = 0.08, which agrees the smaller ionic size of Pb^{2+} (1.29 Å) compared to Bi^{3+}. The presence of secondary phase was confirmed by SEM for $x \geq 0.08$ compositions (**Supplementary Figure 42-45**).

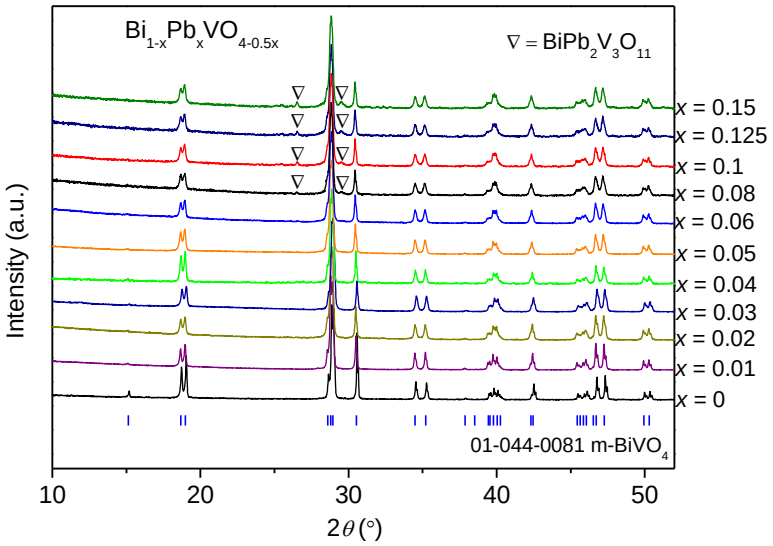

Supplementary Figure 41. XRD patterns of $Bi_{1-x}Pb_xVO_{4-0.5x}$ (x = 0-0.15) samples. The blue vertical ticks denote Bragg reflection positions for the monoclinic $BiVO_4$ (*No.* 01-044-0081) from ICDD database. The ∇ donates the secondary phase $BiPb_2V_3O_{11}$.

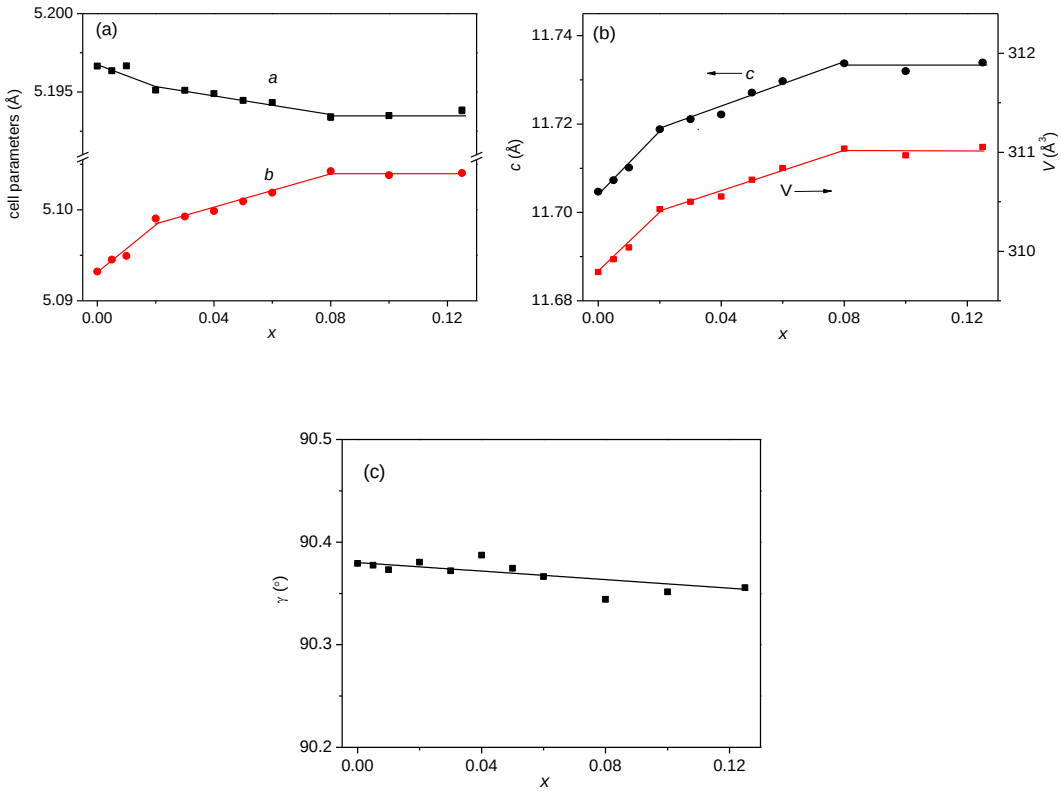

Supplementary Figure 42. The x dependency of the lattice parameters in $Bi_{1-x}Pb_xVO_{4-0.5x}$ (x = 0-0.08).

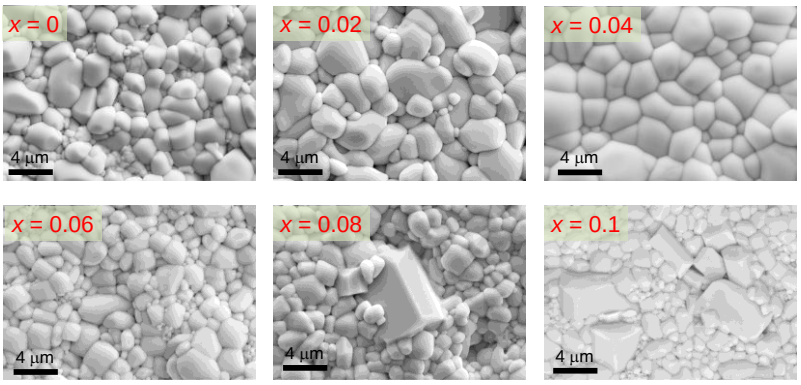

Supplementary Figure 43. The surface morphology of the $Bi_{1-x}Pb_xVO_{4-0.5x}$ (x=0-0.1) ceramic pellets.

Supplementary Figure 44. SEM-EDS elemental mapping of $Bi_{0.94}Pb_{0.06}VO_{3.97}$ ceramic pellet.

Supplementary Figure 45. SEM-EDS elemental mapping of $Bi_{0.94}Pb_{0.08}VO_{3.96}$ ceramic pellet.

Supplementary Note 2.

Phase stability range with temperature. VT-XRD experiment was carried out on *t*-$Bi_{0.85}Ca_{0.15}VO_{3.925}$ to examine its thermal stability and structure evolution. The VT-XRD patterns (**Supplementary Figure 46**) evidenced that the tetragonal Scheelite phase is stable within the whole temperature range analyzed (25-750 ℃) on both heating and cooling. The temperature dependences of the refined lattice parameters (**Supplementary Figure 47**) demonstrate linear expansion behavior without existence of phase transition. Therefore, the Ca doping allows the stabilization of the tetragonal phase by conventional solid-state reaction method, in contrast to the Sr-doping case in which the tetragonal phase can be only accessible through the melt crystallization route.[4]

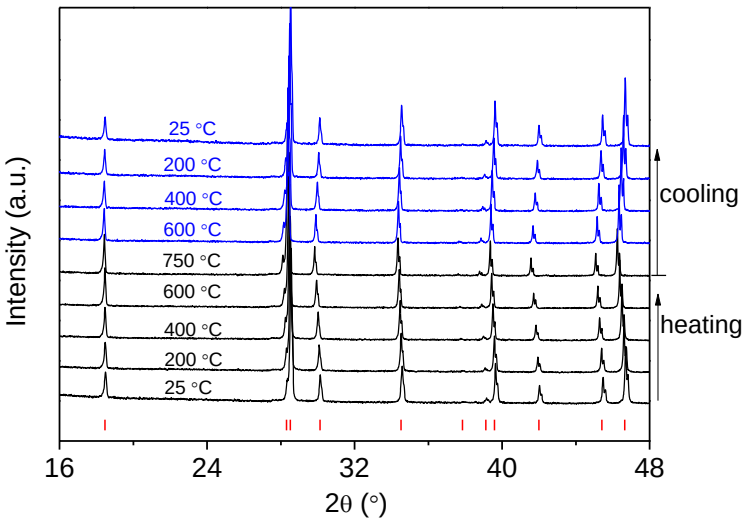

Supplementary Figure 46. VT-XRD patterns of $Bi_{0.85}Ca_{0.15}VO_{3.925}$ powder on heating and cooling. The black and blue lines denote the experimental diffraction data during heating and cooling, respectively. The red vertical bars donate the Bragg reflections of tetragonal Scheelite $BiVO_4$ phase with $I4_1/a$ space group.

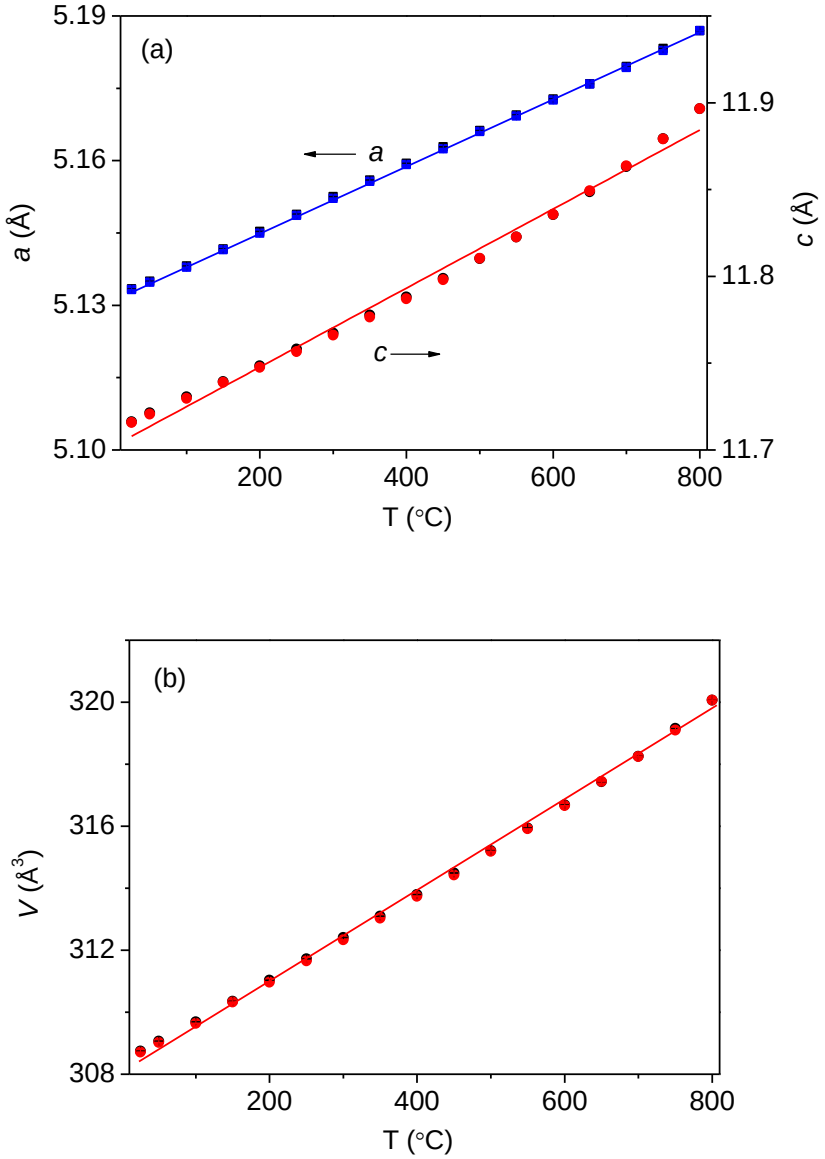

Supplementary Figure 47. Temperature dependence of cell parameters of $Bi_{0.85}Ca_{0.15}VO_{3.925}$ measured by high temperature XRD. *a* and *c* lattice parameters are shown in (a), the unit cell volume is shown in (b).

Supplementary Note 3. Solid solubility discussion.

There exist many factors governing a complete solid solution formation. Humer-Rothery[8] provided the next simple rules to understand the conditions under which an element could replace another one:

1. The atomic radius of elements involved in the substitution process must not differ more than 15%.

2. The crystal structures of solute and solvent phases must be similar.

3. Solvent and solute should have the same valence.

4. The solute and solvent should have similar electronegativity.

In our case, the crystal structures of the end members in the solid solution (i.e., $BiVO_4$ and A_2O_3 oxides) are completely different and, moreover, we employed aliovalent doping strategy to create oxygen vacancies. The analysis of Pauling electronegativities (Supplementary Table 5) does not indicate any strong correlation between the experimental solid solubility range observed as a function of the dopant. Therefore, we will never observe full solid solutions, being their corresponding limits mainly addressed by the ionic size mismatch among the elements.

Supplementary Table 5.

Ionics	Size difference (Å)	Experimental Solid solution limit (mole)	Pauling Electronegativity[9]
Bi^{3+}	-	-	2.02
Mg^{2+}	-0.28	0	1.31
Ca^{2+}	-0.05	0.15	1.00
Cd^{2+}	-0.07	0.08	1.69
Sr^{2+}	+0.09	0.10	0.95
Pb^{2+}	+0.12	0.06	2.33
Ba^{2+}	+0.25	0.02	0.89
V^{5+}	-	-	1.63
Ge^{4+}	+0.035	0.08	2.01
Ti^{4+}	+0.065	0	1.54
Si^{4+}	-0.095	0	1.90

Supplementary References

1. T. S. Bush, J. D. Gale, C. R. A. Catlow and P. D. Battle, Self-consistent interatomic potentials for the simulation of binary and ternary oxides *Journal of Materials Chemistry*, 1994, **4**, 831-837.
2. X. Yang, S. Liu, F. Lu, J. Xu and X. Kuang, Acceptor doping and oxygen vacancy migration in layered perovskite $NdBaInO_4$-based mixed conductors, *Journal of Physical Chemistry C*, 2016, **120**, 6416-6426.
3. Q. Wang, S. Liu, X. Wang, H. Fu, J. Xu, F. Lu, E. Veron, M. Allix, F. Porcher and X. Kuang, Aliovalent-substitution defect chemistry, crystalline-glassy phase separation and ionic conductivity in fresnoite $Ba_2TiSi_2O_8$-based materials, *Solid State Ionics*, 2015, **278**, 157-165.
4. X. Yang, A. J. Fernandez-Carrion, J. Wang, F. Porcher, F. Fayon, M. Allix and X. Kuang, Cooperative mechanisms of oxygen vacancy stabilization and migration in the isolated tetrahedral anion scheelite structure, *Nature Communications*, 2018, **9**, 4484.
5. G. V. Lewis and C. Catlow, Potential models for ionic oxides, *Journal of Physics C: Solid State Physics*, 1985, **18**, 1149-1161.
6. J. Wang, L. Zhou, Y. Wang, J. Xu, X. Yang and X. Kuang, Molecular dynamic simulation of interstitial oxide ion migration in $Pb_{1-x}La_xWO_{4+x/2}$ scheelite, *Journal of Solid State Chemistry*, 2018, **268**, 16-21.
7. S. Uma, R. Bliesner and A. W. Sleight, Oxygen ion conductivity in new oxygen deficient phases with scheelite related structures, *Solid State Sciences*, 2002, **4**, 329-333.
8. W. Hume-Rothery and G. Evans, The freezing points, melting points, and solid solubility limits of the alloys of silver, and copper with the elements of the B sub-groups, *Philosophical Transactions of the Royal Society of London*, 1934, **233**, 1-97.
9. S. Atkins, *Inorganic Chemistry, Fifth edition*, Oxford University Press, 2010.